

<https://helda.helsinki.fi>

COSINE-100 and DAMA/LIBRA-phase2 in WIMP effective models

COSINE-100 Collaboration

2019-06

COSINE-100 Collaboration , Sogang Phenomenology Grp , Adhikari , G & Yoon , J-H 2019 ,
' COSINE-100 and DAMA/LIBRA-phase2 in WIMP effective models ' , Journal of Cosmology
and Astroparticle Physics , no. 6 , 048 . <https://doi.org/10.1088/1475-7516/2019/06/048>

<http://hdl.handle.net/10138/305156>

<https://doi.org/10.1088/1475-7516/2019/06/048>

other

acceptedVersion

Downloaded from Helda, University of Helsinki institutional repository.

This is an electronic reprint of the original article.

This reprint may differ from the original in pagination and typographic detail.

Please cite the original version.

COSINE–100 and DAMA/LIBRA-phase2 in WIMP effective models

The COSINE-100 Collaboration

G. Adhikari^a P. Adhikari^{a,1} E. Barbosa de Souza^b N. Carlin^c
 S. Choi^d M. Djamal^e A. C. Ezeribe^f C. Ha^g I. S. Hahn^h E. J. Jeon^g
 J. H. Jo^b H. W. Joo^d W. G. Kang^g W. Kangⁱ M. Kauer^j
 G. S. Kim^k H. Kim^g H. J. Kim^k K. W. Kim^g N. Y. Kim^g S. K. Kim^d
 Y. D. Kim^{g,a,m} Y. H. Kim^{g,l,m} Y. J. Ko^g V. A. Kudryavtsev^f
 H. S. Lee^{g,m} J. Lee^g J. Y. Lee^k M. H. Lee^{g,m} D. S. Leonard^g
 W. A. Lynch^f R. H. Maruyama^b F. Mouton^f S. L. Olsen^g
 B. J. Park^m H. K. Parkⁿ H. S. Park^l K. S. Park^g R. L. C. Pitta^c
 H. Prihtiadi^e S. J. Ra^g C. Rottⁱ K. A. Shin^g A. Scarff^f
 N. J. C. Spooner^f W. G. Thompson^b L. Yang^o and G. H. Yuⁱ
 The Sogang Phenomenology Group
 Sunghyun Kang^{aa} Stefano Scopel^{aa} Gaurav Tomar^{aa} and
 Jong-Hyun Yoon^{aa,bb}

^aDepartment of Physics, Sejong University, Seoul 05006, Republic of Korea

^bDepartment of Physics and Wright Laboratory, Yale University, New Haven, CT 06520, USA

^cPhysics Institute, University of São Paulo, 05508-090, São Paulo, Brazil

^dDepartment of Physics and Astronomy, Seoul National University, Seoul 08826, Republic of Korea

^eDepartment of Physics, Bandung Institute of Technology, Bandung 40132, Indonesia

^fDepartment of Physics and Astronomy, University of Sheffield, Sheffield S3 7RH, United Kingdom

^gCenter for Underground Physics, Institute for Basic Science (IBS), Daejeon 34126, Republic of Korea

^hDepartment of Science Education, Ewha Womans University, Seoul 03760, Republic of Korea

ⁱDepartment of Physics, Sungkyunkwan University, Suwon 16419, Republic of Korea

^jDepartment of Physics and Wisconsin IceCube Particle Astrophysics Center, University of Wisconsin-Madison, Madison, WI 53706, USA

¹Present address : Department of Physics, Carleton University, Ottawa, ON K1S 5B6, Canada

^kDepartment of Physics, Kyungpook National University, Daegu 41566, Republic of Korea

^lKorea Research Institute of Standards and Science, Daejeon 34113, Republic of Korea

^mIBS School, University of Science and Technology (UST), Daejeon 34113, Republic of Korea

ⁿDepartment of Accelerator Science, Korea University, Sejong 30019, Republic of Korea

^oDepartment of Physics, University of Illinois at Urbana-Champaign, Urbana, IL 61801, USA

^{aa}Department of Physics, Sogang University, Seoul 04107, Republic of Korea

^{bb}Department of Physics, University of Helsinki, FI-00014 Helsinki, Finland

E-mail: scopel@sogang.ac.kr, changhyon.ha@gmail.com

Abstract. Assuming a standard Maxwellian for the WIMP velocity distribution, we obtain the bounds from null WIMP search results of 59.5 days of COSINE-100 data on the DAMA/LIBRA-phase2 modulation effect within the context of the non-relativistic effective theory of WIMP-nucleus scattering. Here, we systematically assume that one of the effective operators allowed by Galilean invariance dominates in the effective Hamiltonian of a spin-1/2 dark matter (DM) particle. We find that, although DAMA/LIBRA and COSINE-100 use the same sodium-iodide target, the comparison of the two results still depends on the particle-physics model. This is mainly due to two reasons: i) the WIMP signal spectral shape; ii) the expected modulation fractions, when the upper bound on the time-averaged rate in COSINE-100 is converted into a constraint on the annual modulation component in DAMA/LIBRA. We find that the latter effect is the dominant one. For several effective operators the expected modulation fractions are larger than in the standard spin-independent or spin-dependent interaction cases. As a consequence, compatibility between the modulation effect observed in DAMA/LIBRA and the null result from COSINE-100 is still possible for several non-relativistic operators. At low WIMP masses such relatively high values of the modulation fractions arise because COSINE-100 is mainly sensitive to WIMP-sodium scattering events, due to the higher threshold compared to DAMA/LIBRA. A next COSINE analysis is expected to have a full sensitivity for the 5σ region of DAMA/LIBRA.

Contents

1	Introduction	1
2	WIMP–nucleus scattering rates in non–relativistic effective models	2
3	Analysis	5
4	Conclusions	15

1 Introduction

Since its first presentation, the DAMA/NaI, DAMA/LIBRA–phase1 and DAMA/LIBRA–phase2’s (DAMA for short) observation [1–4] of an annual modulation signal [5, 6] detected in an array of low–background sodium–iodide crystals has produced continuous speculation about whether or not it is caused by dark matter. Given the substantial statistical significance ($> 10\sigma$) of the signal, an independent verification of the result with the same sodium–iodide, or NaI(Tl) target crystals is required. Experimental efforts by several groups using the same target medium are on–going and in a few years will confirm the presence of the signal in a model–independent way [7–10]. On the other hand, a Weakly Interacting Massive Particle (WIMP) [11, 12] dark-matter interpretations for the positive signal have been ruled out by other experiments [13–16] using time-averaged rates and shapes in the specific context of the Standard Galactic Halo Model [17, 18], assuming a standard spin–independent (SI) or spin–dependent (SD) interaction.

Although preliminary modulation analyses from ANAIS [19] and COSINE-100 [20] have been released, these experiments need several more years of data-taking [21] before they can reach the modulation sensitivity required to probe the DAMA signal. In the meantime, the yearly modulation amplitude and the time–averaged rate can be compared in the context of specific models of WIMP–nucleus interactions. The first such analysis using 59.5 days of COSINE-100 data has excluded the SI WIMP case as a potential model for the DAMA signal interpretation [7].

Since COSINE-100 uses the same target material, fewer assumptions about how the WIMP elastic scattering rates scale with the target nucleus are needed in order to interpret the result. The dominance of WIMP–sodium or WIMP–iodine scattering events for different WIMP masses can then be determined entirely by kinematics. As a consequence, expected rates can be directly expressed in terms of WIMP–nucleus cross sections. For example, this enabled the Korea Invisible Mass Search (KIMS) experiment, using a CsI(Tl) target, to constrain in a model–independent way WIMP–iodine scattering events in DAMA for WIMP masses above approximately $20\text{ GeV}/c^2$ [13]. On the other hand, for lower WIMP masses, where only WIMP–sodium events are kinematically accessible, the DAMA result could only be probed using different target nuclei. Moreover, the recent DAMA/LIBRA–phase2 result with a lower threshold at 1 keV electron-equivalent (keVee), is more sensitive to WIMP–iodine scattering events for WIMP masses below $20\text{ GeV}/c^2$ and the expected relative numbers of WIMP–iodine and WIMP–sodium scattering events is model dependent. To address these aspects, we use non–relativistic (NR) effective field theory in an interpretation of the DAMA signal with the COSINE–100 data.

COSINE-100 [22–24] is a joint dark matter search experiment of KIMS [25–27] and DM-Ice [28, 29] with an array of low radioactive NaI(Tl) crystals at the Yangyang underground laboratory. The experiment is composed of eight encapsulated NaI(Tl) crystals (a total of 106 kg) placed in the middle of a copper box which is filled with 2 tons of liquid scintillator [30] and further shielded by lead and plastic scintillator panels from external radiations. The plastic scintillator panels veto cosmic-ray muons and liquid scintillator actively reduces background radiations that originate from crystals or vicinity of the crystal detectors [23]. The details of the COSINE-100 experimental setup and analysis methods can be found elsewhere [7, 27]. Here, we extend the interpretation of the data collected in Ref. [7] to the general NR effective theory of nuclear scattering for a WIMP of spin 1/2.

The paper is organized by the following structure: Section 2 summarizes the theory of WIMP–nucleus scattering in the NR effective theory of a particle of spin 1/2; Section 3 is devoted to our quantitative analysis; Section 4 contains our conclusions.

2 WIMP–nucleus scattering rates in non-relativistic effective models

The expected rate in a given visible energy bin $E'_1 \leq E' \leq E'_2$ of a direct detection experiment is given by:

$$R_{[E'_1, E'_2]}(t) = MT_{exp} \int_{E'_1}^{E'_2} \frac{dR}{dE'}(t) dE' \quad (2.1)$$

$$\frac{dR}{dE'}(t) = \sum_T \int_0^\infty \frac{dR_{\chi T}(t)}{dE_{ee}} \mathcal{G}_T(E', E_{ee}) \epsilon(E') dE_{ee} \quad (2.2)$$

$$E_{ee} = q(E_R)E_R, \quad (2.3)$$

with $\epsilon(E') \leq 1$ the experimental efficiency/acceptance. In the equations above E_R is the recoil energy deposited in the scattering process (indicated in keVnr), while E_{ee} (indicated in keVee) is the fraction of E_R that goes into the experimentally detected process (ionization, scintillation, heat) and $q(E_R)$ is the quenching factor, $\mathcal{G}_T(E', E_{ee} = q(E_R)E_R)$ is the probability that the visible energy E' is detected when a WIMP has scattered off an isotope T in the detector target with recoil energy E_R , M is the fiducial mass of the detector and T_{exp} the live-time exposure of the data taking.

For a given recoil energy imparted to the target the differential rate for the WIMP–nucleus scattering process is given by:

$$\frac{dR_{\chi T}}{dE_R}(t) = \sum_T N_T \frac{\rho_{\text{WIMP}}}{m_{\text{WIMP}}} \int_{v_{min}} d^3v_T f(\vec{v}_T, t) v_T \frac{d\sigma_T}{dE_R}, \quad (2.4)$$

where ρ_{WIMP} is the local WIMP mass density in the neighborhood of the Sun, N_T the number of the nuclear targets of species T per unit mass in the detector (the sum over T applies in the case of more than one target), while

$$\frac{d\sigma_T}{dE_R} = \frac{2m_T}{4\pi v_T^2} \left[\frac{1}{2j_\chi + 1} \frac{1}{2j_T + 1} |\mathcal{M}_T|^2 \right], \quad (2.5)$$

where m_T is the nuclear target mass and the squared amplitude in parenthesis is given explicitly in Eq.(2.7).

$\mathcal{O}_1 = 1_\chi 1_N$	
$\mathcal{O}_2 = (v^\perp)^2$	$\mathcal{O}_9 = i\vec{S}_\chi \cdot (\vec{S}_N \times \frac{\vec{q}}{m_N})$
$\mathcal{O}_3 = i\vec{S}_N \cdot (\frac{\vec{q}}{m_N} \times \vec{v}^\perp)$	$\mathcal{O}_{10} = i\vec{S}_N \cdot \frac{\vec{q}}{m_N}$
$\mathcal{O}_4 = \vec{S}_\chi \cdot \vec{S}_N$	$\mathcal{O}_{11} = i\vec{S}_\chi \cdot \frac{\vec{q}}{m_N}$
$\mathcal{O}_5 = i\vec{S}_\chi \cdot (\frac{\vec{q}}{m_N} \times \vec{v}^\perp)$	$\mathcal{O}_{12} = \vec{S}_\chi \cdot (\vec{S}_N \times \vec{v}^\perp)$
$\mathcal{O}_6 = (\vec{S}_\chi \cdot \frac{\vec{q}}{m_N})(\vec{S}_N \cdot \frac{\vec{q}}{m_N})$	$\mathcal{O}_{13} = i(\vec{S}_\chi \cdot \vec{v}^\perp)(\vec{S}_N \cdot \frac{\vec{q}}{m_N})$
$\mathcal{O}_7 = \vec{S}_N \cdot \vec{v}^\perp$	$\mathcal{O}_{14} = i(\vec{S}_\chi \cdot \frac{\vec{q}}{m_N})(\vec{S}_N \cdot \vec{v}^\perp)$
$\mathcal{O}_8 = \vec{S}_\chi \cdot \vec{v}^\perp$	$\mathcal{O}_{15} = -(\vec{S}_\chi \cdot \frac{\vec{q}}{m_N})(\vec{S}_N \times \vec{v}^\perp) \cdot \frac{\vec{q}}{m_N}$

Table 1. Non-relativistic Galilean invariant operators for dark matter with spin 1/2.

WIMP–nucleus scattering is a non-relativistic process that can be fully described in a non-relativistic Effective Theory approach. In the case of a spin-1/2 DM particle the corresponding Hamiltonian density is given by [31, 32]:

$$\mathcal{H}(\mathbf{r}) = \sum_{\tau=0,1} \sum_{j=1}^{15} c_j^\tau \mathcal{O}_j(\mathbf{r}) t^\tau, \quad (2.6)$$

where, \mathcal{O}_j ’s are non-relativistic Galilean invariant operators which have been collected in Table 1. In the same Table 1_χ and 1_N are identity operators, \vec{q} is the transferred momentum, \vec{S}_χ and \vec{S}_N are the WIMP and nucleon spins, respectively, while $\vec{v}^\perp = \vec{v} + \frac{\vec{q}}{2\mu_T}$ (with μ_T the WIMP–nucleus reduced mass) is the relative transverse velocity operator satisfying $\vec{v}^\perp \cdot \vec{q} = 0$. In particular, one has $(v_T^\perp)^2 = v_T^2 - v_{min}^2$, where, for WIMP–nucleus elastic scattering, $v_{min}^2 = \frac{q^2}{4\mu_T^2} = \frac{m_T E_R}{2\mu_T^2}$ represents the minimal incoming WIMP speed required to impart the nuclear recoil energy E_R , while $v_T \equiv |\vec{v}_T|$ is the WIMP speed in the reference frame of the nuclear center of mass. Moreover $t^0 = 1$, $t^1 = \tau_3$ denote the 2×2 identity and third Pauli matrix in isospin space, respectively, and the isoscalar and isovector (dimension -2) coupling constants c_j^0 and c_j^1 , are related to those for protons and neutrons c_j^p and c_j^n by $c_j^p = (c_j^0 + c_j^1)$ and $c_j^n = (c_j^0 - c_j^1)$.

Operator \mathcal{O}_2 is of higher order in v compared to all the others, implying a cross section suppression of order $\mathcal{O}(v/c)^4) \simeq 10^{-12}$ for the non-relativistic WIMPs in the halo of our Galaxy. Moreover it cannot be obtained from the leading-order non-relativistic reduction of a manifestly relativistic operator [31]. So, following Refs.[31, 32], we will not include it in our analysis.

Assuming that the nuclear interaction is the sum of the interactions of the WIMPs with the individual nucleons in the nucleus the WIMP scattering amplitude on the target nucleus T can be written in the compact form:

$$\frac{1}{2j_\chi + 1} \frac{1}{2j_T + 1} |\mathcal{M}|^2 = \frac{4\pi}{2j_T + 1} \sum_{\tau=0,1} \sum_{\tau'=0,1} \sum_k R_k^{\tau\tau'} \left[c_j^\tau, c_j^{\tau'}, (v_T^\perp)^2, \frac{q^2}{m_N^2} \right] W_{Tk}^{\tau\tau'}(y). \quad (2.7)$$

In the above expression j_χ and j_T are the WIMP and the target nucleus spins, respectively, $q = |\vec{q}|$ while the $R_k^{\tau\tau'}$ ’s are WIMP response functions (that can be found in Ref. [32]) which

$\mathbf{c_j}$	$R_{0k}^{\tau\tau'}$	$R_{1k}^{\tau\tau'}$	$\mathbf{c_j}$	$R_{0k}^{\tau\tau'}$	$R_{1k}^{\tau\tau'}$
c_1	$M(q^0)$	-	c_3	$\Phi''(q^4)$	$\Sigma'(q^2)$
c_4	$\Sigma''(q^0), \Sigma'(q^0)$	-	c_5	$\Delta(q^4)$	$M(q^2)$
c_6	$\Sigma''(q^4)$	-	c_7	-	$\Sigma'(q^0)$
c_8	$\Delta(q^2)$	$M(q^0)$	c_9	$\Sigma'(q^2)$	-
c_{10}	$\Sigma''(q^2)$	-	c_{11}	$M(q^2)$	-
c_{12}	$\Phi''(q^2), \tilde{\Phi}'(q^2)$	$\Sigma''(q^0), \Sigma'(q^0)$	c_{13}	$\tilde{\Phi}'(q^4)$	$\Sigma''(q^2)$
c_{14}	-	$\Sigma'(q^2)$	c_{15}	$\Phi''(q^6)$	$\Sigma'(q^4)$

Table 2. Nuclear response functions corresponding to each coupling c_j of the effective Hamiltonian (2.6), for the velocity-independent and the velocity-dependent components parts of the WIMP response function, decomposed as in Eq.(2.8). In parenthesis the power of q in the WIMP response function.

depend on the couplings c_j^τ as well as the transferred momentum \vec{q} and $(v_T^\perp)^2$. In equation (2.7) the $W_{Tk}^{\tau\tau'}(y)$'s are nuclear response functions and the index k represents different effective nuclear operators, which, crucially, under the assumption that the nuclear ground state is an approximate eigenstate of P and CP , can be at most eight: following the notation in [31, 32], $k=M, \Phi'', \Phi''M, \tilde{\Phi}', \Sigma'', \Sigma', \Delta, \Delta\Sigma'$. The $W_{Tk}^{\tau\tau'}(y)$'s are function of $y \equiv (qb/2)^2$, where b is the size of the nucleus. For the target nuclei T used in most direct detection experiments the functions $W_{Tk}^{\tau\tau'}(y)$, calculated using nuclear shell models, have been provided in Refs.[32, 33]¹. The correspondence between models and nuclear response functions can be directly read off from the WIMP response functions $R_k^{\tau\tau'}$ [32]. In particular, using the decomposition:

$$R_k^{\tau\tau'} = R_{0k}^{\tau\tau'} + R_{1k}^{\tau\tau'}(v_T^\perp)^2 = R_{0k}^{\tau\tau'} + R_{1k}^{\tau\tau'}(v_T^2 - v_{min}^2), \quad (2.8)$$

such correspondence is summarized for convenience in Table 2.

Finally, $f(\vec{v}_T)$ is the WIMP velocity distribution, for which we assume a standard isotropic Maxwellian at rest in the Galactic rest frame truncated at the escape velocity u_{esc} , and boosted to the Lab frame by the velocity of the Earth. So, for the former we assume:

$$f(\vec{v}_T, t) = N \left(\frac{3}{2\pi v_{rms}^2} \right)^{3/2} e^{-\frac{3|\vec{v}_T + \vec{v}_E|^2}{2v_{rms}^2}} \Theta(u_{esc} - |\vec{v}_T + \vec{v}_E(t)|) \quad (2.9)$$

$$N = \left[\text{erf}(z) - \frac{2}{\sqrt{\pi}} z e^{-z^2} \right]^{-1}, \quad (2.10)$$

with $z = 3u_{esc}^2/(2v_{rms}^2)$. In the isothermal sphere model hydrothermal equilibrium between the WIMP gas pressure and gravity is assumed, leading to $v_{rms} = \sqrt{3/2}v_0$ with v_0 the galactic rotational velocity. The yearly modulation effect is due to the time dependence of the Earth's speed with respect to the Galactic frame:

¹Setting $k = M$ and $W_{TM}^{p,n}(q) \equiv (W_{TM}^{00}(q) \pm W_{TM}^{01}(q) \pm W_{TM}^{10}(q) + W_{TM}^{11}(q))/4$, in the case of a standard spin-independent interaction one has $16/(2j_T + 1)W_{TM}^p(q) = Z_T^2 F^2(q)$ and $16/(2j_T + 1)W_{TM}^n(q) = (A_T - Z_T)^2 F^2(q)$, with Z_T and $A_T - Z_T$ the number of protons and neutrons in target T , and $F(q)$ the SI nuclear form factor, for which the parameterization in [34] is commonly assumed.

$$|\vec{v}_E(t)| = v_{Sun} + v_{orb} \cos \gamma \cos \left[\frac{2\pi}{T_0}(t - t_0) \right], \quad (2.11)$$

where $\cos \gamma \simeq 0.49$ accounts for the inclination of the ecliptic plane with respect to the Galactic plane, $T_0=1$ year, $t_0=2$ June, $v_{orb}=2\pi r_\oplus/(T_0) \simeq 29$ km/sec ($r_\oplus=1$ AU, neglecting the small eccentricity of the Earth's orbit around the Sun) while $v_{Sun}=v_0+12$ km/sec, accounting for a peculiar component of the solar system with respect to the galactic rotation. For the two parameters v_0 and u_{esc} we take $v_0=220$ km/sec [35] and $u_{esc}=550$ km/sec [36]. In the isothermal model the time dependence of Eq. (2.11) induces an expected rate with the functional form $S(t) = S_0 + S_m \cos(2\pi/T - t_0)$, with $S_m > 0$ at large values of v_{min} and turning negative when $v_{min} \lesssim 200$ km/s. In such regime of v_{min} and below the phase is modified by the focusing effect of the Sun's gravitational potential [37], while when $S_m \ll S_0$ the time dependence differs from a simple cosine due the contribution of higher harmonics [6].

In particular, in each visible energy bin DAMA is sensitive to the yearly modulation amplitude S_m , defined as the cosine transform of $R_{[E'_1, E'_2]}(t)$:

$$S_{m,[E'_1, E'_2]} \equiv \frac{2}{T_0} \int_0^{T_0} \cos \left[\frac{2\pi}{T_0}(t - t_0) \right] R_{[E'_1, E'_2]}(t) dt, \quad (2.12)$$

while other experiments put upper bounds on the time average S_0 :

$$S_{0,[E'_1, E'_2]} \equiv \frac{1}{T_0} \int_0^{T_0} R_{[E'_1, E'_2]}(t) dt. \quad (2.13)$$

In the present paper, we will systematically consider the possibility that one of the couplings c_j dominates in the effective Hamiltonian of Eq. (2.6). In this case it is possible to factorize a term $|c_j^p|^2$ from the squared amplitude of Eq.(2.7) and express it in terms of the *effective* WIMP–proton cross section:

$$\sigma_p = (c_j^p)^2 \frac{\mu_{\chi\mathcal{N}}^2}{\pi}, \quad (2.14)$$

(with $\mu_{\chi\mathcal{N}}$ the WIMP–nucleon reduced mass) and the ratio $r \equiv c_j^n/c_j^p$. It is worth pointing out here that among the generalized nuclear response functions arising from the effective Hamiltonian (2.6) only the ones corresponding to M (SI interaction), Σ'' and Σ' (both related to the standard spin–dependent interaction) do not vanish for $q \rightarrow 0$, and so allow to interpret σ_p in terms of a long–distance, point–like cross section. In the case of the other interactions Φ'' , $\tilde{\Phi}'$ and Δ the quantity σ_p is just a convenient alternative to directly parameterizing the interaction in terms of the c_j^p coupling. Since we will not consider interferences among different couplings the response functions $W_{T_k}^{\tau\tau'}(y)$ for $k=\Phi''M, \Delta\Sigma'$ will not play any role in our analysis.

3 Analysis

This analysis uses the COSINE-100 data from October 20, 2016 to December 19, 2016. After application of data quality criteria, the 59.5 live days of good data are used for the results presented here. A total of 11 hours of data did not pass these quality requirement where abrupt high PMT noise triggers and electronic interference triggers were rejected. Total exposure is 6303.9 kg·day. During this period, light yield, gain, and other environmental

c_j	$m_{\chi,\min}$ (GeV)	$r_{\chi,\min}$	σ (cm ²)	χ^2_{\min}
c_1	11.17	-0.76	2.67e-38	11.38
	45.19	-0.66	1.60e-39	13.22
c_3	8.10	-3.14	2.27e-31	11.1
	35.68	-1.10	9.27e-35	14.23
c_4	11.22	1.71	2.95e-36	11.38
	44.71	-8.34	5.96e-36	27.7
c_5	8.34	-0.61	1.62e-29	10.83
	96.13	-5.74	3.63e-34	11.11
c_6	8.09	-7.20	5.05e-28	11.11
	32.9	-6.48	5.18e-31	12.74
c_7	13.41	-4.32	4.75e-30	13.94
	49.24	-0.65	1.35e-30	38.09
c_8	9.27	-0.84	8.67e-33	10.82
	42.33	-0.96	1.30e-34	11.6
c_9	9.3	4.36	8.29e-33	10.69
	37.51	-0.94	1.07e-33	15.23
c_{10}	9.29	3.25	4.74e-33	10.69
	36.81	0.09	2.25e-34	12.40
c_{11}	9.27	-0.67	1.15e-34	10.69
	38.51	-0.66	9.17e-37	13.02
c_{12}	9.26	-2.85	3.92e-34	10.69
	35.22	-1.93	2.40e-35	12.47
c_{13}	8.65	-0.26	1.21e-26	10.76
	29.42	0.10	5.88e-29	14.28
c_{14}	10.28	-0.59	2.61e-26	11.21
	38.88	-1.93	2.19e-27	14.48
c_{15}	7.32	-3.58	2.04e-27	12.91
	33.28	4.25	2.05e-33	16.26

Table 3. Absolute and local minima of the DAMA-phase2 modulation result χ^2 of Eq.(3.12) for each of the couplings c_j of the effective Hamiltonian (2.6). From Ref. [38].

data show stable behavior. The overall crystal PMT gain is changed by less than 1% relative to the beginning of the physics run.

An event is triggered if a photon is observed in each PMT within 200 ns in a crystal. When this happens the data acquisition system reads out the full veto detectors including liquid scintillator and plastic scintillators and other crystal signals simultaneously [24]. The detector stability is checked by using crystal internal gamma calibrations which show consistent results with external source calibrations. The low energy electron signals produced from ^{60}Co calibration of the Compton scattering and tagged by neighboring crystals are used to separate the PMT noise events from data.

First, muon-induced events are rejected by requiring the time difference between muon veto events in the plastic panels and the crystal to be less than 30 ms. This efficiently removes

$\mathbf{c_j}$	$\left(\frac{S_m^{DAMA}}{S_0^{DAMA}}\right)_{E' < 3.5 \text{ keVee}}$		$\mathbf{c_j}$	$\left(\frac{S_m^{DAMA}}{S_0^{DAMA}}\right)_{E' < 3.5 \text{ keVee}}$	
	Low-mass local minimum	High-mass local minimum		Low-mass local minimum	High-mass local minimum
c_1	0.066	0.054	c_3	0.120	0.098
c_4	0.065	0.047	c_5	0.122	0.059
c_6	0.121	0.111	c_7	0.097	0.080
c_8	0.094	0.072	c_9	0.093	0.079
c_{10}	0.093	0.085	c_{11}	0.094	0.083
c_{12}	0.094	0.096	c_{13}	0.123	0.139
c_{14}	0.126	0.122	c_{15}	0.146	0.113

Table 4. Minimum value of the modulation fraction $(S_m^{DAMA}/S_0^{DAMA})_{E' < 3.5 \text{ keVee}}$ in the three DAMA energy bins for $2 \text{ keVee} \leq E' \leq 3.5 \text{ keVee}$, where the bulk of the DAMA modulation effect above the COSINE-100 threshold is concentrated

most of muon-induced events that directly pass through the crystals. We, then, require that leading edges of the trigger pulses start later than $2.0 \mu\text{s}$, each waveform contain more than two pulses, and integrated charge below the baseline should be small enough. These reject muon-induced phosphor events and electronic interference events. Next, we demand a single-site condition where neighboring crystals should not have more than four photons and an energy deposit by the surrounding liquid scintillator should be less than 20 keV.

To identify scintillation signals, one must reject two types of backgrounds which are more than the desired signals especially below 20 keVee region. The first class is thin pulses that are originated from PMTs. These noise events are triggered partly from the PMT individually and partly from radioactivities inside the PMT circuitry which make the crystal scintillate. The second class, less often than the first, consists of bell-shaped waveforms that occur sporadically and in a few PMTs only. These bell-shaped pulses are produced due to occasional PMT discharge and the shape of a waveform looks more symmetric than a typical scintillation signal.

The initial rejection algorithms focus on eliminating the thin pulses and other pathological events. We calculate the balance of the deposited charge from two PMTs (Asymmetry : Eq. 3.1 shown in a) of Fig. 1), the charge fraction of 500 ns to 600 ns from the first 600 ns (X1 : Eq. 3.2 shown in b) of Fig. 1), the charge fraction of the first 50 ns to first 600 ns (X2 : Eq. 3.3 shown in c) of Fig. 1), the charge-weighted mean time of pulses within first 500 ns (MT : Eq. 3.6 shown in e) of Fig. 1), the total charge (QC : Eq. 3.10) and the number of pulses (NC : Eq. 3.9). Boosted Decision Trees (BDTs) were trained using aforementioned variables. The electron/gammas signal model is obtained from the energy-weighted ^{60}Co multiple-site distributions and data is used for the noise model. Each crystal is trained for a separate BDT. Six parameters comparing noise-containing data with ^{60}Co multiple signals are shown in Fig. 1.

The definitions of each variable used in the rejection algorithms are following,

$$Asymmetry = (Q_1 - Q_2)/(Q_1 + Q_2) \quad (3.1)$$

$$X1 = \sum_{100\ ns}^{600\ ns} q_i / \sum_{0\ ns}^{600\ ns} q_i \quad (3.2)$$

$$X2 = \sum_{0\ ns}^{50\ ns} q_i / \sum_{0\ ns}^{600\ ns} q_i \quad (3.3)$$

$$X3 = \sum_{0\ ns}^{120\ ns} q_i / \sum_{0\ ns}^{600\ ns} q_i \quad (3.4)$$

$$X4 = \sum_{100\ ns}^{150\ ns} q_i / \sum_{0\ ns}^{600\ ns} q_i \quad (3.5)$$

$$MT = \sum_{0\ ns}^{500\ ns} q_i t_i / \sum_{0\ ns}^{500\ ns} q_i \quad (3.6)$$

$$MTL = \sum_{0\ ns}^{30\ ns} q_i t_i / \sum_{0\ ns}^{30\ ns} q_i \quad (3.7)$$

$$MV = \sum_{0\ ns}^{1000\ ns} q_i t_i^2 / \sum_{0\ ns}^{1000\ ns} q_i - \left(\sum_{0\ ns}^{1000\ ns} q_i t_i / \sum_{0\ ns}^{1000\ ns} q_i \right)^2 \quad (3.8)$$

$$NC = \text{the number of pulses} \quad (3.9)$$

$$QC = \sum_{0\ ns}^{5000\ ns} q_i \quad (3.10)$$

$$CAT = \text{time of 95\% charge accumulation} \left(\sum_{0\%}^{95\%} q_i \right), \quad (3.11)$$

where $Q_{1,2}$ indicates PMT integrated charges within $5\ \mu s$ and q_i and t_i are waveform amplitudes and times for each $2\ ns$ bin, respectively.

For the rejection of the bell-shaped pulse events in the Crystal-1 in the later quarter of the data, we trained another BDT (BDTA) using the variance of charge-weighted mean time (MV : Eq. 3.8), the charge ratios of waveform leading edges (X3 : Eq. 3.4 shown in d) of Fig. 1 and X4 : Eq. 3.5), the charge-weighted mean time (MT : Eq. 3.6 and MTL : Eq. 3.7), the charge accumulation time (CAT : Eq. 3.11 shown in f) of Fig. 1) and the energy of the event. These effectively identify the shape distortion compared to the regular scintillation signals. Unlike the previous BDT training, early three quarter of the Crystal-1 data as a good data and the later quarter of the data as a noise-contained data are used for signal and background in the training process and later the same training BDT output is applied to all other crystals.

The single-site event spectrum is obtained after the application of the selection criteria and their efficiencies are measured from the ^{60}Co multiples. On average, event selection efficiency of 70% at 2 keVee is obtained for six crystals except Crystal-5 and Crystal-8 which show higher energy threshold at 4 keVee and 8 keVee, respectively, due to their low light yield. The progression of event selection for Crystal-7 is shown in Fig. 2.

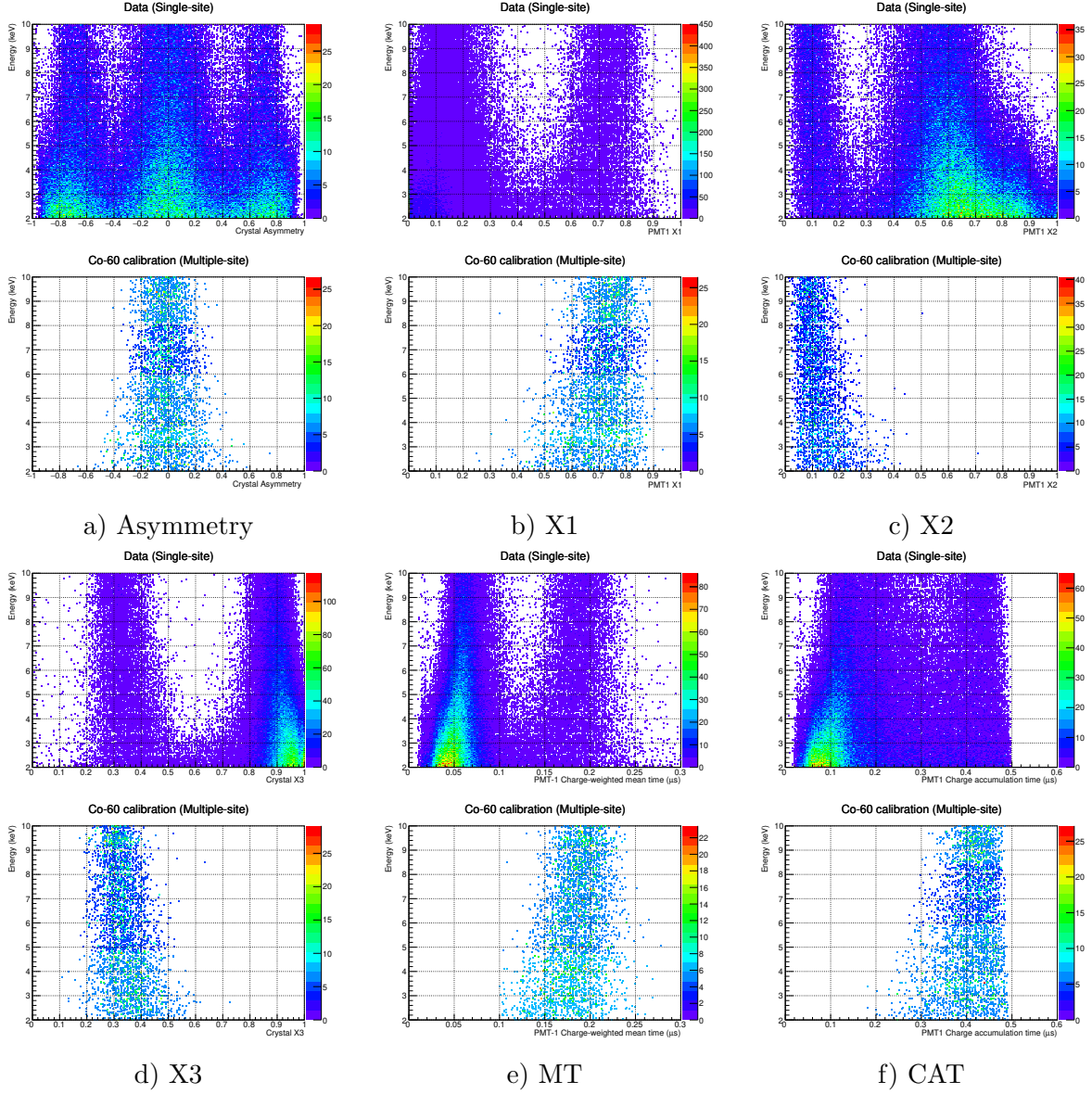


Figure 1. Selective input parameters for training BDTs. All parameters are drawn as a function of energy between 2 and 10 keV. The upper panel of each parameter is showing noise-contained data while the lower panel shows calibration signal which contains no noise.

The selection efficiency of these event selections are separately checked with neutron-induced nuclear recoils obtained with a small rectangular (2 cm×2 cm×1.5 cm) NaI(Tl) crystals from the same ingots of the detector crystals in front of 2.42 MeV mono-energetic neutron beams [39]. The efficiency of nuclear recoil events in energies between 2 and 20 keV is consistent with the ^{60}Co calibration efficiency, which indicates that the selections do not affect the possible WIMP signal region.

To compare the results of COSINE-100 and DAMA/LIBRA-phase2 we start from the best-fit analysis of the DAMA/LIBRA-phase2 modulation effect in terms of NR WIMP effective models in Ref. [38], as summarized in Table 3. In such table each of the NR

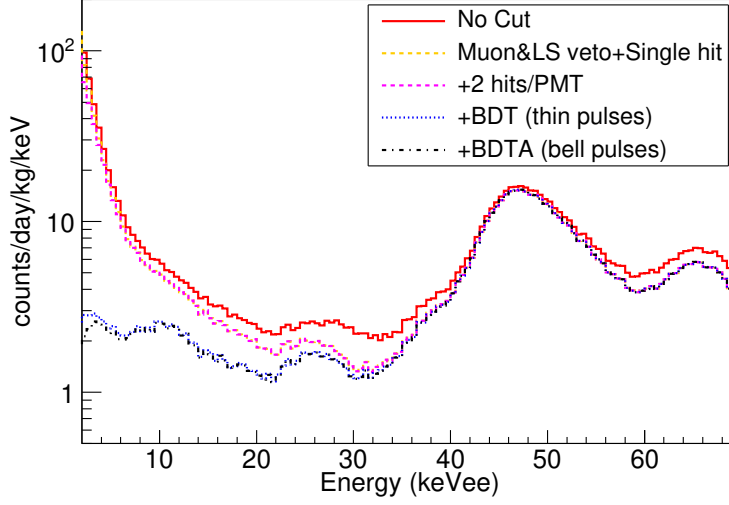


Figure 2. Staged event selection versus energy. The low-energy spectrum between 2 and 70 keVee is displayed with the progression of application of the selection criteria. The selection efficiency is uncorrected here.

couplings is assumed to be the only term in the effective Hamiltonian of Eq. (2.6) and the χ^2 :

$$\chi^2(m_\chi, \sigma_p, r) = \sum_{k=1}^{15} \frac{[S_{m,k}(m_\chi, \sigma_p, r) - S_{m,k}^{exp}]^2}{\sigma_k^2} \quad (3.12)$$

(where we consider 14 energy bins, of 0.5 keVee width, from 1 keVee to 8 keVee, and one high-energy control bin from 8 keVee to 16 keVee) is minimized in terms of the WIMP mass m_χ , the neutron-over-proton coupling ratio $r \equiv c^n/c^p$ and of the effective cross section σ_p as defined in Eq. (2.14). In Eq. (3.12) $S_{m,k} \equiv S_{m,[E'_k, E'_{k+1}]}$ is given by Eq. (2.12), while $S_{m,k}^{exp}$ and σ_k represent the modulation amplitudes and $1\text{-}\sigma$ uncertainties as measured by DAMA/LIBRA-phase2 [4] and reported in Table 5.

As shown in Table 3 for each NR coupling two local minima of the χ^2 are found (low and high-mass) with the low-mass solution corresponding in all cases to the absolute minimum. With the exception of the high-mass minima for the \mathcal{O}_4 and \mathcal{O}_7 operators, all the χ^2 minima of Table 3 are acceptable with $15 - 3$ degrees of freedom. In particular, the DAMA/LIBRA-phase2 has lowered the energy threshold to 1 keVee, implying that it is sensitive to WIMP-iodine scattering events for WIMP masses below $\simeq 20 \text{ GeV}/c^2$. In the SI case this requires to highly tune the parameters to suppress the iodine contribution, in order to avoid an otherwise too steeply increasing spectrum at low energy of the modulation amplitudes compared to the data [40]. On the other hand, if the WIMP-nucleus cross section is driven by other operators the fine tuning required to suppress iodine is reduced and/or the hierarchy between the WIMP-iodine and the WIMP-sodium cross section is less pronounced in the first place [38].

The raw and observed WIMP spectra corresponding to the best-fit values of Table 3 for operators $c_1\text{--}c_{15}$ are shown in Fig. 3. The raw spectra are generated by using Eq. (2.4), while the energy resolutions obtained from individual crystal measurements and the DAMA

Energy (keVee)	$S_{m,k}$	σ_k
1.0 – 1.5	0.0242	0.0056
1.5 – 2.0	0.0211	0.0043
2.0 – 2.5	0.0179	0.0023
2.5 – 3.0	0.0197	0.0030
3.0 – 3.5	0.0186	0.0027
3.5 – 4.0	0.0110	0.0026
4.0 – 4.5	0.0109	0.0021
4.5 – 5.0	0.0032	0.0019
5.0 – 5.5	0.0065	0.0019
5.5 – 6.0	0.0059	0.0019
6.0 – 6.5	0.0010	0.0016
6.5 – 7.0	0.0008	0.0017
7.0 – 7.5	0.0009	0.0016
7.5 – 8.0	0.0009	0.0016
8.0 – 16.0	0.0003	0.0004

Table 5. Combination of the DAMA/LIBRA–phase1 and the DAMA/LIBRA–phase2 measurements for the modulation amplitudes $S_{m,k}$ with statistical errors σ_k used in the present analysis (from Ref. [4]).

quenching factors (0.3 for Na and 0.09 for I) are applied to the raw signal to create the WIMP signal models.

To test the presence of a WIMP signal in the COSINE–100 data that is consistent to the modulation effect measured by DAMA/LIBRA, we generated WIMP spectra for 5 mass values centered around each of the low–mass and high–mass modulation minima of Table 3.

To extract the WIMP signal from our data, a Bayesian approach with a likelihood function based on the Poisson probability is used. A WIMP is not expected to have multiple scatterings within our detector volume, so our WIMP search window is the 2–20 keVee region in the single–hit spectrum where the average event rate of all crystal is recorded to 3.5 counts/day/kg/keV. All crystals are fitted together with crystal-specific background models and a single WIMP signal at a given mass. The constraints are applied as 1σ Gaussian priors for those obtained from the background understanding. Similarly, systematic parameters that change the shape of the background distributions are added as nuisance parameters.

In this way for each NR coupling and WIMP mass value we produce a posterior probability of the effective cross section σ_p . Examples of the posterior probability versus σ_p are provided in Fig. 4 for the couplings c_1 , c_3 and c_{13} . For all the couplings c_1 – c_{15} we find no signal, so a 90% confidence level (C.L.) upper limit is obtained by integrating the posterior probability from zero.

The result of our analysis is summarized in Figs. 5 and 6 where, for each NR effective coupling, the DAMA modulation regions at $1\text{--}\sigma$, $3\text{--}\sigma$ and $5\text{--}\sigma$ is compared to the COSINE–100 90% C.L. exclusion limit in the m_χ – σ_p plane. The present analysis is focused on the comparison between DAMA and COSINE-100. However, it is worth reminding here that limits from detectors using target materials different from *NaI* exclude effective cross sections ranging from one to three orders of magnitude below the DAMA region [38].

In each plot of Fig. 5 the neutron–over–proton coupling ratio $r = c^n/c^p$ is fixed to the

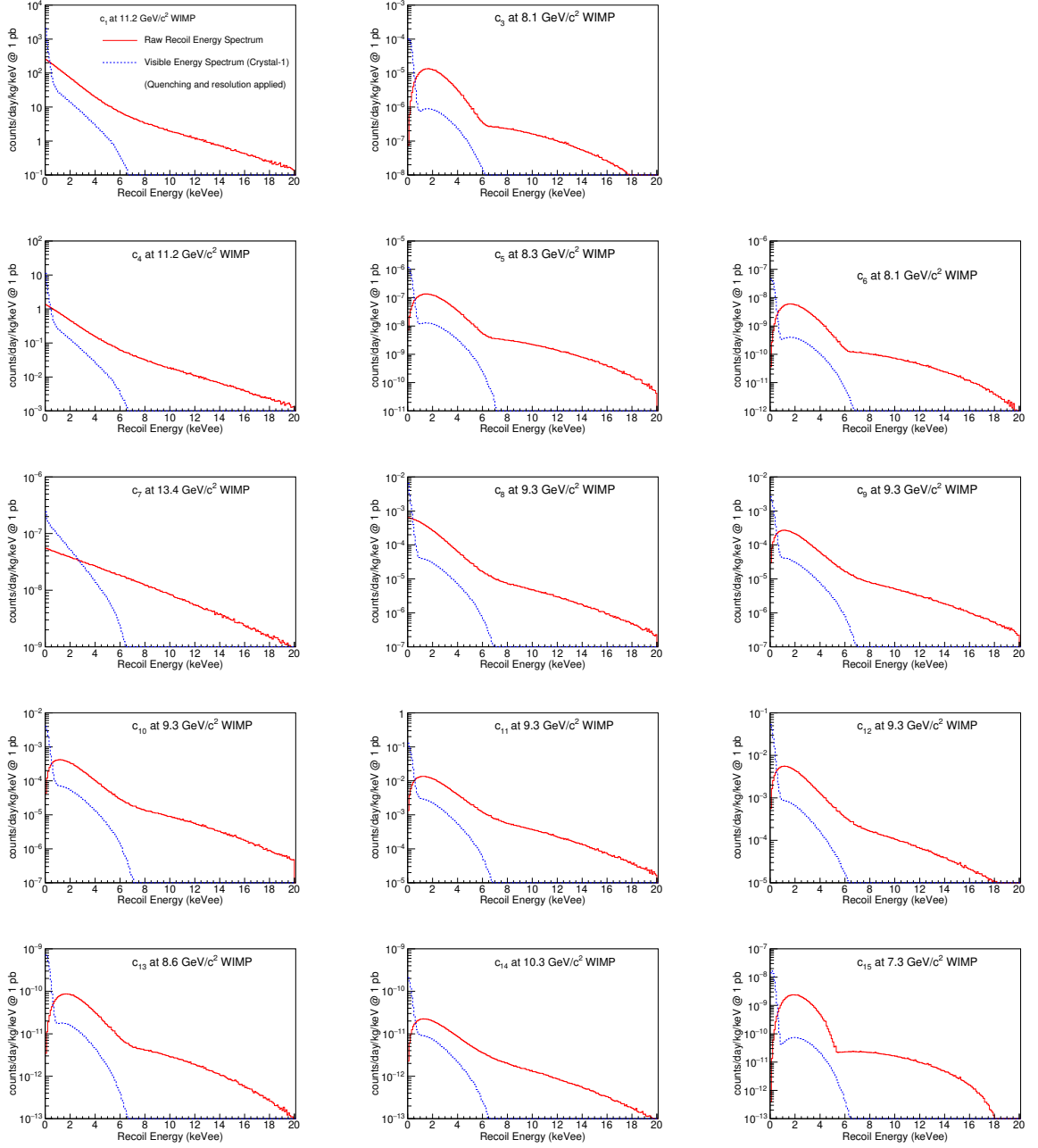


Figure 3. Count rate versus recoil energy spectrum. Raw energy spectra for the case of couplings c_1 – c_{15} at their best fit low-mass positions are compared to the visible energy spectra at Crystal-1 where the DAMA quenching factor and the crystal resolution are applied. The event rate is normalized to a unit of counts/day/kg/keV assuming 1 picobarn cross-section. The largest impact is from the quenching factor. After the 2 keVee threshold is applied for the analysis, the effect from the iodine component is largely negligible.

corresponding low-mass best-fit value of Table 3 and the WIMP mass interval is centered accordingly. In Fig. 6 the same is done for the high-mass best fit values of Table 3 (in the latter figure the cases of couplings c_4 and c_7 are not included since they do not provide a

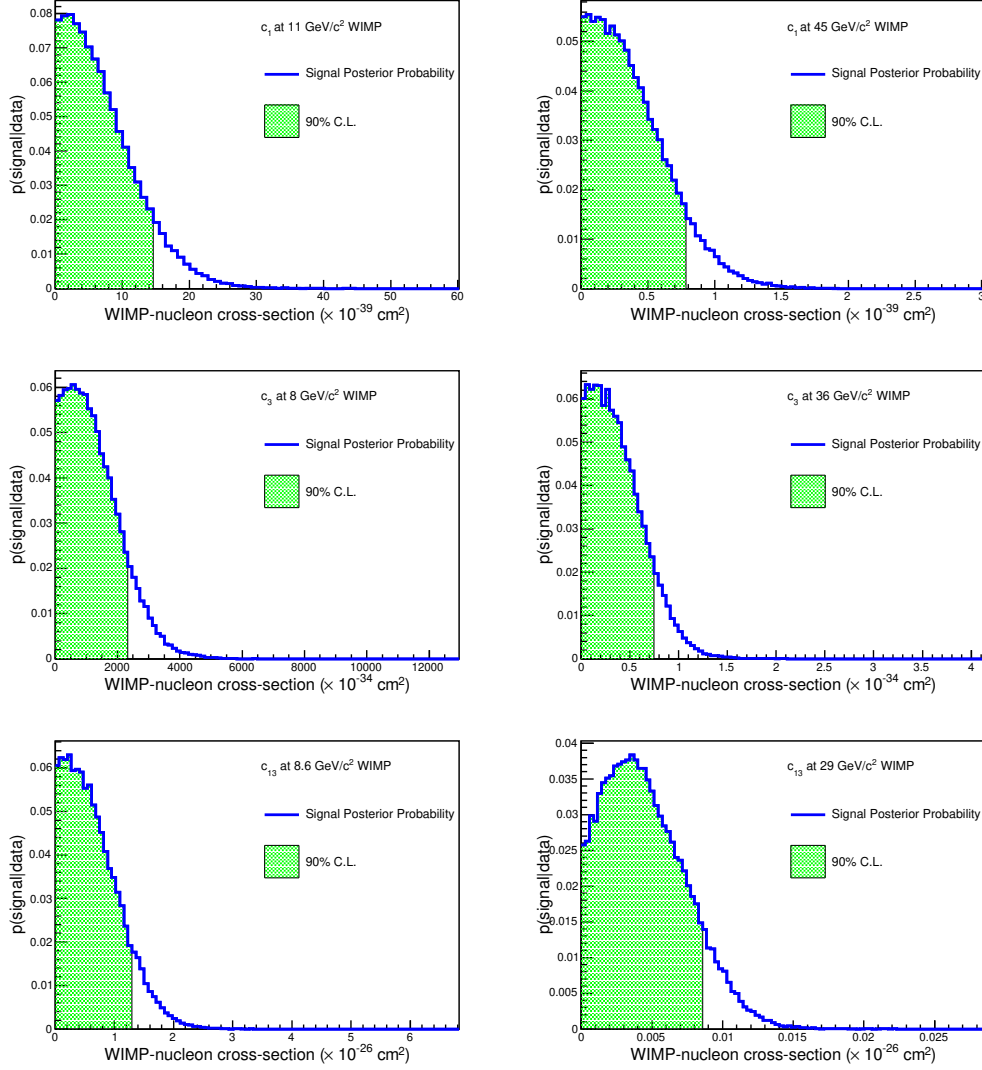


Figure 4. Posterior probability versus signal strength for selective operators; c_1 , c_3 and c_{13} . A posterior probability of a signal given data are drawn as a function of WIMP-nucleon cross-section scaled at 10^{-39} cm^2 , 10^{-34} cm^2 and 10^{-26} cm^2 respectively for c_1 , c_3 and c_{13} . No signal is observed for those WIMP mass points. Therefore, 90% confidence level (C.L.) limit was obtained by integrating the probability from zero. For the high mass case of c_{13} , a positive 0.9σ fluctuation in the mean of the probability is observed implying a weaker bound.

good fit to the DAMA modulation amplitudes).

Figs. 5-6 show that the exclusion plot on σ_p from COSINE-100 has a different impact on the DAMA best fit modulation region depending on the specific non-relativistic model. Namely, as far as the DAMA low-mass minima of Fig. 5 are concerned, the tension between DAMA/LIBRA and COSINE-100 is maximal for the couplings c_1 and c_4 , while for the DAMA high-mass minima of Fig. 6 this happens for the couplings c_1 and c_8 : in all such cases the 90% C.L. bound from COSINE-100, represented by the (blue) solid line, rules out all the 5-sigma DAMA region shown as the (red) dot-dashed contour. On the other hand, in

all other cases the 5-sigma DAMA region is not completely excluded by the corresponding 90% C.L. COSINE-100 upper bound, with two instances (c_{15} at low WIMP mass c_{13} at high WIMP mass) for which all the DAMA modulation region is allowed by the COSINE-100 constraint.

The main motivation of probing the modulation effect claimed by DAMA/LIBRA using a sodium-iodide target with COSINE-100 is to obtain results that depend as little as possible on the unknown properties of the WIMP particle. On the other hand, the model dependence observed in Figs. 5–6 is due to two main reasons: i) the change in the signal spectral shape; ii) the expected modulation fractions $S_{m,[E'_1,E'_2]}/S_{0,[E'_1,E'_2]}$ in DAMA.

As far as the spectral shape of the expected WIMP signal is concerned, each of the effective models listed in Table 1 is characterized by a different dependence on the exchanged momentum q (and so on the recoil energy $E_R = q^2/(2m_T)$), both through the nuclear response functions $W_{Tk}(q)$ (with $k=M, \Phi'', \tilde{\Phi}', \Sigma'', \Sigma', \Delta$) and through additional powers of q in the scattering amplitude (as summarized in Table 2). The raw energy spectra in COSINE-100 calculated using Eq. (2.4) are shown with a red solid line in Fig. 3 for each NR operator. Indeed, while in the standard spin-independent and spin-dependent cases (corresponding to c_1 and c_4) the expected differential rate is the featureless superposition of two exponentially decaying spectra due to WIMP-iodine and WIMP-sodium scattering events, in the case of other NR operators the WIMP recoil spectrum can show a maximum at low energy that may mimic one of the observed radiation peaks (such as the one due to ^{40}K) potentially affecting the sensitivity to the signal. However, as shown in Fig. 3 with the blue dotted lines, when the quenching factors for Na and I and the crystal resolution are applied to the raw spectra all the expected rates are compressed to lower visible energies, so that this effect is strongly reduced. Moreover the expected rates in COSINE-100 become almost insensitive to WIMP-iodine scattering events, that are driven below the 2 keVee threshold. An example of this effect is provided by the c_{13} coupling for which a slight 0.9σ positive fluctuation from zero is observed in the posterior probability, weakening the bound as shown in Fig. 6. This may be partially ascribed to the shape of the signal spectrum, as shown in Fig. 3.

However, a much more important source of model dependence in Figs. 5 and 6 is due to the modulation fractions. In fact, the data used in the present paper (and in the result of Ref. [7]) are sensitive to the time-averaged count rate, so that they are used to put upper bounds on the quantity $S_{0,[E'_1,E'_2]}$ defined in Eq. (2.13). On the other hand, the DAMA effect WIMP interpretation is in terms of the $S_{m,[E'_1,E'_2]}$ quantities of Eq. (2.12). Crucially, the ratio of the two quantities depends both on the WIMP velocity distribution (for which we assume here a standard Maxwellian as given in Eq. (2.10)) and on the specific operator assumed to dominate in the Hamiltonian of Eq. (2.6) among those in Table 1. The variation of the modulation fraction with the NR model is shown in Table 4, where for each NR operator we provide the minimum value of the modulation fraction $(S_m^{DAMA}/S_0^{DAMA})_{E' < 3.5 \text{ keVee}}$ in the three DAMA energy bins for $2 \text{ keVee} \leq E' \leq 3.5 \text{ keVee}$, where the bulk of the DAMA modulation effect above the COSINE-100 threshold is concentrated. Such variations are an effect of the same modified spectral features discussed in Fig. 3. In particular, larger modulation fractions appear for WIMP scattering events off sodium targets, which are sensitive to the high-speed tail of the velocity distribution, and when the scattering amplitude is multiplied by powers of the transferred momentum q (as summarized in Table 2) due to the enhanced dependence of the expected rate on the v_{min} parameter.

One can notice that in the same energy intervals of Table 4 the time-averaged spectrum in DAMA is above $\simeq 0.8$ events/day/kg/keVee (see Fig. 1 in [4]). An analysis of

the DAMA unmodulated data similar to the one that we perform in the present paper for COSINE-100 is not available and beyond our capability (since it would require a detailed understanding of the background, possibly from Monte Carlo simulations, and access to the systematics of the experiment). If, instead, a vanishing background is conservatively assumed in DAMA, no constraint on the modulation effect can be obtained. In fact the minimal modulation fraction of Table 4 ($\simeq 0.065$ events/kg/day/keVee) implies an upper bound $S_m \lesssim 0.05$ events/kg/day/keVee, which is above the corresponding measured values of the modulated amplitudes (see Table 5).

As far as COSINE-100 is concerned, a given upper bound on the time-averaged rate S_0 is converted into a bound on the yearly modulated component S_m in DAMA whose strength is inversely proportional to the expected modulated fraction S_m/S_0 . In Table 4 one can see that the smallest values for $(S_m^{DAMA}/S_0^{DAMA})_{E' < 3.5 \text{ keVee}}$ (and so the strongest limits on the modulated amplitudes) correspond to the standard SI and SD couplings (c_1 and c_4) at the level of about 7%. Indeed, as shown in Figs. 5 and 6 such values are small enough for the corresponding COSINE-100 exclusion plots to exclude all the DAMA 5- σ region. However, for several models (c_3 , c_5 , c_6 , c_{13} and c_{14} at low WIMP mass and c_{14} at high WIMP mass) the modulation fraction $(S_m^{DAMA}/S_0^{DAMA})_{E' < 3.5 \text{ keVee}}$ is as high as $\simeq 12\%$, and about half of the corresponding 5 sigma C.L. DAMA regions are allowed. For most other models the modulation fraction is at an intermediate value $\simeq 0.10$ so that most of the DAMA 5-sigma region is excluded. Notice that the two highest numerical values in Table 4 ($\simeq 0.14$ for the high-mass DAMA best-fit of c_{13} and $\simeq 0.15$ for the low-mass DAMA best-fit of c_{15}) correspond to the two less-constraining cases in Figs. 5 and 6 for which all the DAMA modulation region is allowed by the COSINE-100 bound. Therefore, the lower energy threshold of COSINE-100 would improve the bound at low WIMP masses because WIMP-iodine scattering events in the energy range $1 \text{ keVee} \leq E' \leq 2 \text{ keVee}$ drive S_m/S_0 to lower values. The case of c_5 in Fig. 6 is a peculiar one: as discussed in [38] the corresponding effective operator leads to a velocity-dependent cross section for which the χ -square can saturate to a constant, acceptable value at large WIMP masses. This explains the peculiar elongated shape for c_5 in Fig. 6.

4 Conclusions

Assuming a standard Maxwellian for the WIMP velocity distribution, in the present paper we have discussed the bounds from the null WIMP search result of the COSINE-100 experiment on the DAMA/LIBRA-phase2 modulation effect within the context of the non-relativistic effective theory of WIMP-nucleus scattering. To this aim we have systematically assumed that one of the effective operators allowed by Galilean invariance dominates in the effective Hamiltonian of a spin-1/2 DM particle.

We find that, although DAMA/LIBRA and COSINE-100 use the same sodium-iodide target, the comparison of the two results still depends on the particle-physics model. This is mainly due to two reasons: i) the WIMP signal spectral shape; ii) the expected modulation fractions, when the upper bound on the time-averaged rate in COSINE-100 is converted into a constraint on the yearly modulated component in DAMA/LIBRA. We find that the latter effect is the dominant one. In particular, for several effective operators we find that the expected modulation fractions are larger than in the standard spin-independent or spin-dependent interaction cases. As a consequence, for such operators compatibility between the modulation effect observed in DAMA/LIBRA and the null result from COSINE-100 is

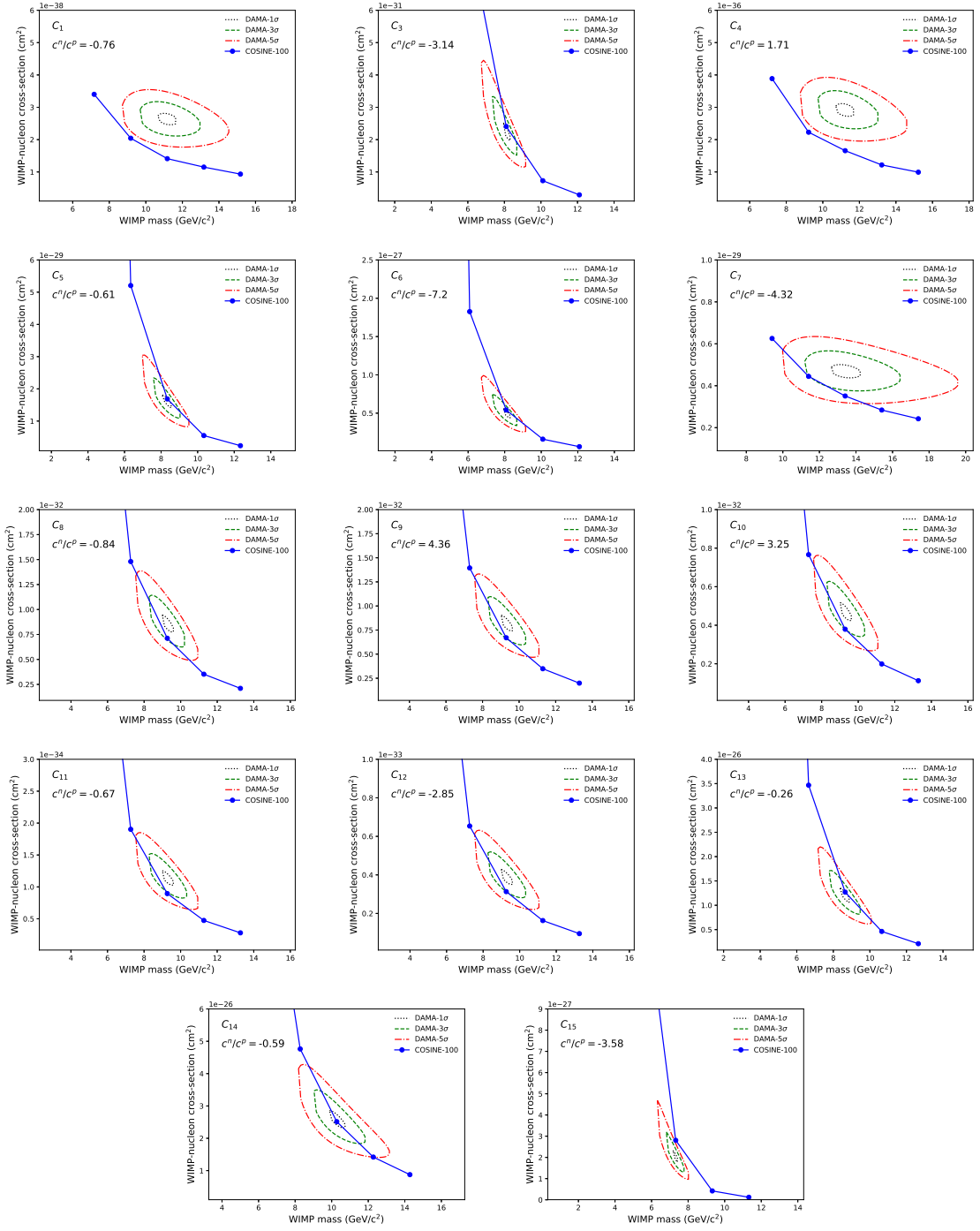


Figure 5. Low WIMP mass DAMA modulation region ($1\text{-}\sigma$, $3\text{-}\sigma$ and $5\text{-}\sigma$) and COSINE-100 90% C.L. exclusion plot to the effective WIMP–proton cross section σ_p of Eq. (2.14) for all the 14 NR effective operators of Table 1. For each operator the $r=c^n/c^p$ neutron–over–proton ratio is fixed to the corresponding low–mass best fit value in Table 3.

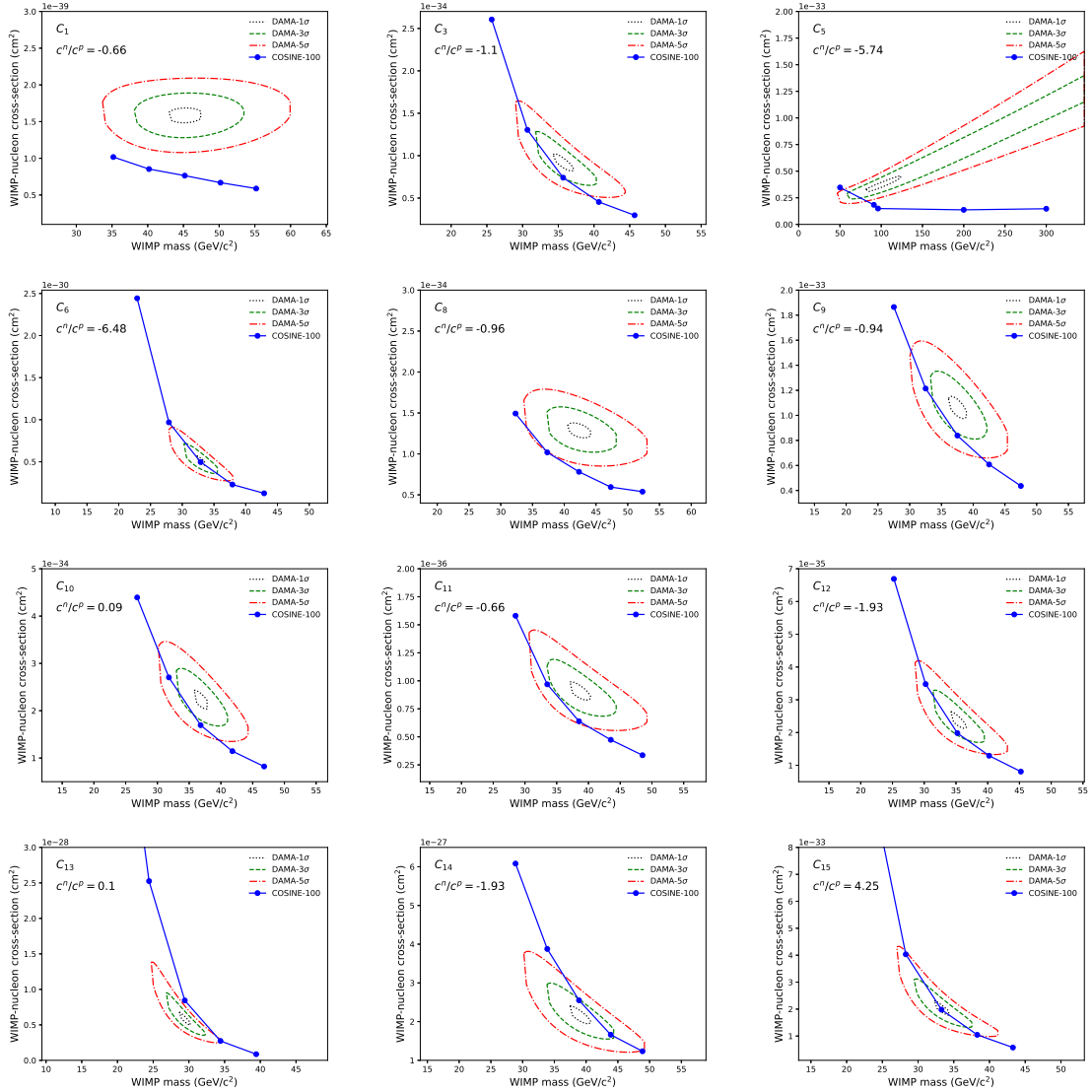


Figure 6. High WIMP mass DAMA modulation region (1- σ , 3- σ and 5- σ) and COSINE-100 90% C.L. exclusion plot to the effective WIMP-proton cross section σ_p of Eq. (2.14) for all the 14 NR effective of Table 1. For each operator the $r=c^n/c^p$ neutron-over-proton ratio is fixed to the corresponding high-mass best fit value in Table 3.

still possible. COSINE-100 has been taking stable data for more than 2.5 years and 1 keVee threshold analysis is forthcoming. This would improve the bound at low WIMP masses because WIMP-iodine scattering events in the energy range $1 \text{ keVee} \leq E' \leq 2 \text{ keVee}$ drive S_m/S_0 to lower values.

Acknowledgments

The Sogang group's research was supported by the Basic Science Research Program through the National Research Foundation of Korea(NRF) funded by the Ministry of Education, grant

number 2016R1D1A1A09917964. Jong-Hyun Yoon acknowledges support from the Magnus Ehrnrooth Foundation. We thank the Korea Hydro and Nuclear Power (KHNP) Company for providing underground laboratory space at Yangyang. The work of COSINE-100 is supported by: the Institute for Basic Science (IBS) under project code IBS-R016-A1, Republic of Korea; UIUC campus research board, the Alfred P. Sloan Foundation Fellowship, NSF Grants No. PHY-1151795, PHY-1457995, DGE-1122492 and DGE-1256259, WIPAC, the Wisconsin Alumni Research Foundation, Yale University and DOE/NNSA Grant No. DE-FC52-08NA28752, United States; STFC Grant ST/N000277/1 and ST/K001337/1, United Kingdom; and Grant No. 2017/02952-0 FAPESP and CAPES Finance Code 001, Brazil.

References

- [1] **DAMA** Collaboration, R. Bernabei et al., *First results from DAMA/LIBRA and the combined results with DAMA/NaI*, *Eur. Phys. J. C* **56** (2008) 333–355, [[arXiv:0804.2741](#)].
- [2] **DAMA, LIBRA** Collaboration, R. Bernabei et al., *New results from DAMA/LIBRA*, *Eur. Phys. J. C* **67** (2010) 39–49, [[arXiv:1002.1028](#)].
- [3] **DAMA** Collaboration, R. Bernabei et al., *Final model independent result of DAMA/LIBRA-phase1*, *Eur. Phys. J. C* **73** (2013) 2648.
- [4] **DAMA** Collaboration, R. Bernabei et al., *First Model Independent Results from DAMA/LIBRAPhase2*, *Nucl. Phys. At. Energy* **19** (2018) 307, [[arXiv:1805.10486](#)].
- [5] C. Savage, G. Gelmini, P. Gondolo, and K. Freese, *Compatibility of DAMA/LIBRA dark matter detection with other searches*, *JCAP* **0904** (2009) 010.
- [6] K. Freese, M. Lisanti, and C. Savage, *Colloquium: Annual modulation of dark matter*, *Rev. Mod. Phys.* **85** (2013) 1561–1581.
- [7] **COSINE-100** Collaboration, G. Adhikari et al., *An experiment to search for dark-matter interactions using sodium iodide detectors*, *Nature* **564** (2018) 83–86.
- [8] **ANAIS** Collaboration, J. Amar et al., *Performance of ANAIS-112 experiment after the first year of data taking*, *Eur. Phys. J. C* **79** (2019), no. 3 228, [[arXiv:1812.01472](#)].
- [9] **SABRE** Collaboration, P. Montini, *Dark matter search with the SABRE experiment*, [[arXiv:1807.08073](#)].
- [10] **COSINUS** Collaboration, G. Angloher et al., *The COSINUS project - perspectives of a NaI scintillating calorimeter for dark matter search*, *Eur. Phys. J. C* **76** (2016), no. 8 441, [[arXiv:1603.02214](#)].
- [11] B. W. Lee and S. Weinberg, *Cosmological Lower Bound on Heavy Neutrino Masses*, *Phys. Rev. Lett.* **39** (1977) 165–168. [,183(1977)].
- [12] M. W. Goodman and E. Witten, *Detectability of Certain Dark Matter Candidates*, *Phys. Rev. D* **31** (1985) 3059. [,325(1984)].
- [13] **KIMS** Collaboration, S. C. Kim et al., *New Limits on Interactions between Weakly Interacting Massive Particles and Nucleons Obtained with CsI(Tl) Crystal Detectors*, *Phys. Rev. Lett.* **108** (2012) 181301.
- [14] **XENON** Collaboration, E. Aprile et al., *Search for electronic recoil event rate modulation with 4 years of xenon100 data*, *Phys. Rev. Lett.* **118** (Mar, 2017) 101101.
- [15] **PandaX** Collaboration, A. Tan et al., *Dark Matter Results from First 98.7 Days of Data from the PandaX-II Experiment*, *Phys. Rev. Lett.* **117** (2016), no. 12 121303.
- [16] **XENON** Collaboration, E. Aprile et al., *First Dark Matter Search Results from the XENON1T Experiment*, *Phys. Rev. Lett.* **119** (2017), no. 18 181301.

- [17] J. Lewin and P. Smith, *Review of mathematics, numerical factors, and corrections for dark matter experiments based on elastic nuclear recoil*, *Astropart. Phys.* **6** (1996) 87–112.
- [18] K. Freese, J. A. Frieman, and A. Gould, *Signal Modulation in Cold Dark Matter Detection*, *Phys. Rev. D* **37** (1988) 3388–3405.
- [19] **ANAIS** Collaboration, J. Amare et al., *First results on dark matter annual modulation from ANAIS-112 experiment*, [arXiv:1903.03973](#).
- [20] **COSINE-100** Collaboration, G. Adhikari et al., *Search for a dark matter-induced annual modulation signal in NaI(Tl) with the COSINE-100 experiment*, [arXiv:1903.10098](#).
- [21] **COSINE-100** Collaboration, W. G. Thompson, *Current status and projected sensitivity of COSINE-100*, in *15th International Conference on Topics in Astroparticle and Underground Physics (TAUP 2017) Sudbury, Ontario, Canada, July 24-28, 2017*, 2017. [arXiv:1711.01488](#).
- [22] **COSINE-100** Collaboration, G. Adhikari et al., *Initial Performance of the COSINE-100 Experiment*, *Eur. Phys. J. C* **78** (2018), no. 2 107.
- [23] **COSINE-100** Collaboration, H. Prihtiadi et al., *Muon detector for the COSINE-100 experiment*, *JINST* **13** (2018), no. 02 T02007.
- [24] **COSINE-100** Collaboration, G. Adhikari et al., *The COSINE-100 Data Acquisition System*, *JINST* **13** (2018), no. 09 P09006, [[arXiv:1806.09788](#)].
- [25] **KIMS** Collaboration, K. W. Kim et al., *Tests on NaI(Tl) crystals for WIMP search at the Yangyang Underground Laboratory*, *Astropart. Phys.* **62** (2015) 249.
- [26] **KIMS** Collaboration, P. Adhikari et al., *Understanding internal backgrounds in NaI(Tl) crystals toward a 200 kg array for the KIMS-NaI experiment*, *Eur. Phys. J. C* **76** (2016), no. 4 185.
- [27] **COSINE-100** Collaboration, G. Adhikari et al., *Understanding NaI(Tl) crystal background for dark matter searches*, *Eur. Phys. J. C* **77** (2017), no. 7 437.
- [28] **DM-Ice** Collaboration, J. Cherwinka et al., *First data from DM-Ice17*, *Phys. Rev. D* **90** (2014) 092005.
- [29] **DM-Ice** Collaboration, E. Barbosa de Souza et al., *First search for a dark matter annual modulation signal with NaI(Tl) in the Southern Hemisphere by DM-Ice17*, *Phys. Rev. D* **95** (2017), no. 3 032006.
- [30] **KIMS** Collaboration, J. S. Park et al., *Performance of a prototype active veto system using liquid scintillator for a dark matter search experiment*, *Nucl. Instrum. Meth. A* **851** (2017) 103–107.
- [31] A. L. Fitzpatrick, W. Haxton, E. Katz, N. Lubbers, and Y. Xu, *The Effective Field Theory of Dark Matter Direct Detection*, *JCAP* **1302** (2013) 004, [[arXiv:1203.3542](#)].
- [32] N. Anand, A. L. Fitzpatrick, and W. C. Haxton, *Weakly interacting massive particle-nucleus elastic scattering response*, *Phys. Rev.* **C89** (2014), no. 6 065501, [[arXiv:1308.6288](#)].
- [33] R. Catena and B. Schwabe, *Form factors for dark matter capture by the Sun in effective theories*, *JCAP* **1504** (2015), no. 04 042, [[arXiv:1501.03729](#)].
- [34] R. H. Helm, *Inelastic and Elastic Scattering of 187-Mev Electrons from Selected Even-Even Nuclei*, *Phys. Rev.* **104** (1956) 1466–1475.
- [35] S. E. Koposov, H.-W. Rix, and D. W. Hogg, *Constraining the Milky Way potential with a 6-D phase-space map of the GD-1 stellar stream*, *Astrophys. J.* **712** (2010) 260–273, [[arXiv:0907.1085](#)].
- [36] T. Piffl et al., *The RAVE survey: the Galactic escape speed and the mass of the Milky Way*, *Astron. Astrophys.* **562** (2014) A91, [[arXiv:1309.4293](#)].

- [37] S. K. Lee, M. Lisanti, A. H. G. Peter, and B. R. Safdi, *Effect of Gravitational Focusing on Annual Modulation in Dark-Matter Direct-Detection Experiments*, *Phys. Rev. Lett.* **112** (2014), no. 1 011301, [[arXiv:1308.1953](#)].
- [38] S. Kang, S. Scopel, G. Tomar, and J.-H. Yoon, *DAMA/LIBRA-phase2 in WIMP effective models*, *JCAP* **1807** (2018), no. 07 016, [[arXiv:1804.07528](#)].
- [39] H. W. Joo, H. S. Park, J. H. Kim, S. K. Kim, Y. D. Kim, H. S. Lee, and S. H. Kim, *Quenching factor measurement for NaI(Tl) scintillation crystal*, *Astropart. Phys.* **108** (2019) 50–56, [[arXiv:1809.10310](#)].
- [40] S. Baum, K. Freese, and C. Kelso, *Dark Matter implications of DAMA/LIBRA-phase2 results*, *Phys. Lett.* **B789** (2019) 262–269, [[arXiv:1804.01231](#)].